

Article

Unveiling the Thermal Behavior of SnS_2 Anodes Across Delithiation Stages

Mahmoud Reda ^{1,2,†}, **Jana Kupka** ^{1,2,3,†}, **Yuri Surace** ³, **Damian M. Cupid** ³ and **Hans Flandorfer** ^{1,*}¹ Department of Functional Materials and Catalysis, University of Vienna, Josef-Holaubek-Platz 2, 1090 Vienna, Austria; mahmoud.reda@univie.ac.at (M.R.); jana.kupka@ait.ac.at (J.K.)² Vienna Doctoral School in Chemistry (DoSChem), University of Vienna, Währinger Straße 42, 1090 Vienna, Austria³ Center for Transport Technologies, AIT Austrian Institute of Technology GmbH, Giefinggasse 4, 1210 Vienna, Austria; yuri.surace@ait.ac.at (Y.S.); damian.cupid@ait.ac.at (D.M.C.)

* Correspondence: hans.flandorfer@univie.ac.at

† These authors contributed equally to this work.

Abstract

This study investigates the thermal behavior of SnS_2 anodes for lithium-ion batteries at seven different states of charge (fully discharged (lithiated) at 0 mAh/g, partially charged at 100, 200, 300, 400, and 500 mAh/g, and fully charged (delithiated) at 550 mAh/g) using differential scanning calorimetry (DSC). To better understand the observed thermal behavior, complementary XRD and XPS analyses were performed. Generally, in all electrodes, the thermal decomposition of the electrode material is initiated by the exothermic decomposition of the SEI followed by a binder decomposition reaction around 265 °C. Interestingly, with increased states of delithiation from 400 mAh/g, endothermic peaks in the heat-flow signal of the DSC measurements are observed, which can be correlated with the structural and compositional changes in the electrode material as determined by XRD and XPS, respectively. These analyses confirmed the progressive formation of metallic tin on advanced delithiation. Additionally, the total heat generation from the electrodes decreased with increased delithiation. The results of this study serve as the basis for better understanding the thermal decomposition of SnS_2 -based anodes, which are considered promising for advanced lithium-ion battery chemistries.



Academic Editor: Xianglin Li

Received: 1 September 2025

Revised: 29 September 2025

Accepted: 10 October 2025

Published: 16 October 2025

Citation: Reda, M.; Kupka, J.; Surace,

Y.; Cupid, D.M.; Flandorfer, H.

Unveiling the Thermal Behavior of

 SnS_2 Anodes Across DelithiationStages. *Batteries* **2025**, *11*, 378. <https://doi.org/10.3390/batteries11100378>**Copyright:** © 2025 by the authors.

Licensee MDPI, Basel, Switzerland.

This article is an open access article distributed under the terms and conditions of the Creative Commons Attribution (CC BY) license (<https://creativecommons.org/licenses/by/4.0/>).

1. Introduction

To keep up with rising demands for the use of energy from sustainable sources for both stationary and mobile applications, both the energy density and specific energy of lithium-ion batteries (LIBs) must be increased. One way to achieve higher volumetric and specific energies is to use anode materials with larger Li capacities than graphite. Graphite stores lithium via an intercalation mechanism, where 6 C atoms are required for the uptake of 1 lithium atom, corresponding to the LiC_6 stoichiometry [1–3]. However, since materials such as silicon, tin, or germanium form alloys with lithium, they achieve higher specific capacities. For example, 4.25 lithium atoms can be stored per tin atom corresponding to the formation of $\text{Li}_{17}\text{Sn}_4$, whereas 3.75 lithium atoms can be stored per silicon atom, corresponding to $\text{Li}_{15}\text{Si}_4$. Due to the higher Li capacities, the use of electroactive materials which uptake Li via the alloying mechanism would lead to thinner and lighter electrodes for LIB manufacturing [4–6].

Tin is one of the prospective alloy-forming materials with a theoretical capacity of 959 mAh/g, which is associated with the formation of $\text{Li}_{17}\text{Sn}_4$. Such lithiated Sn-based anodes are also expected to be more thermodynamically stable than graphite-based electrodes, since $\text{Li}_{17}\text{Sn}_4$ decomposes endothermically at 758 °C [7] compared to LiC_6 's exothermic decomposition at 330 °C [8]. However, the use of alloy-forming materials as anodes for LIBs is severely limited by the volume changes that usually occur during lithiation. In the case of Sn, the alloying reaction results in a ~260% volume expansion between the de-lithiated and fully lithiated states. These volume changes are detrimental to the cycling performance of electrodes due to particle cracking, continuous solid electrolyte interphase (SEI) formation, and loss of connection to the current collector leading to continuous capacity losses [9].

One strategy to mitigate the volume change is the use of active/inactive alloy design, where one phase is electrochemically active, and the other electrochemically inactive component buffers the mechanical stress induced by the volume expansion [10]. The inactive phase can be admixed or precipitated on lithiation by a conversion reaction. In this light, SnS_2 , a layered material based on S-Sn-S triple layers, which crystallizes with a trigonal crystal structure (space group $P\bar{3}m1$, Figure 1), is a potential solution. During lithiation, an inactive Li_2S matrix is formed via the conversion mechanism, which can buffer the mechanical stress induced by volume changes in the electrodes during cycling [11]. Other factors that make SnS_2 a candidate to replace graphite are its high reversible theoretical capacity of 623 mAh/g (1.7 times the theoretical capacity of graphite) [12], low cost, and earth abundance [13]. This earth abundance has become more important recently, since battery-grade graphite is considered a critical raw material [14]. However, due to the irreversible consumption of Li in the formation of the inactive Li_2S matrix, SnS_2 -based materials suffer from low first-cycle coulombic efficiencies (theoretically from 1209 to 623 mAh/g, 48.5% capacity loss), which have inhibited their application in commercial LIB cells.

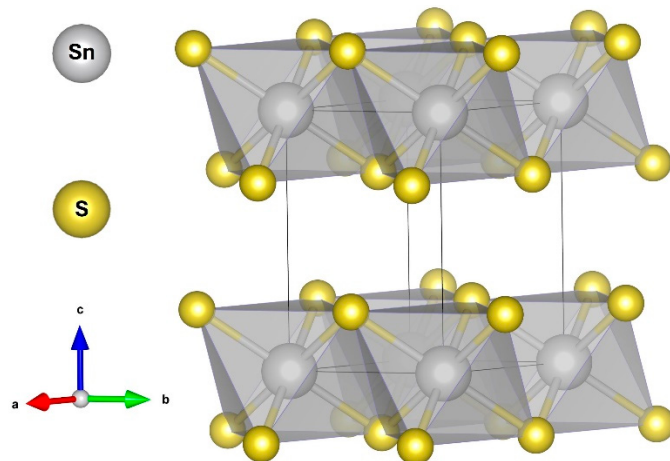


Figure 1. Schematic illustration of SnS_2 's crystal structure. Visualization was performed using VESTA software (V3) [15]. (a,b,c) are the crystallographic axes.

Recently, SnS_2 has been investigated at the laboratory scale as shown by literature studies where the performance of SnS_2 has been improved through making a composite electrode with reduced graphene oxide [16], with nanoscale silicon [17], or multiple-element doping [18]. Additionally, other factors like control of crystallinity [19], particle morphology [20], particle size [21], and pre-lithiation [22] may influence the electrochemical performance of SnS_2 -based electrodes. Nevertheless, the thermal behavior of SnS_2 -based anodes has not yet been adequately explored. In fact, only thermogravimetric analysis has been performed on SnS_2/C composites at the materials level to determine their carbon contents [23,24]. However, understanding the thermal behavior of anodes is important, as

the thermal breakdown and the heat released from the anode are the initiators of thermal runaway [25]. Thus, it is important to determine the heat released from the anode materials at any given state of charge. In addition, the heat released from the anode is a large contributor to the total energy released from a battery during thermal runaway [26]. Hence, understanding and reducing this energy is essential to having a safer battery. Therefore, SnS₂'s unknown thermal stability is a crucial missing piece in evaluating its viability as a graphite alternative.

During lithiation, at capacity ranges of 0–200 mAh/g, SnS₂ forms Li_xSnS₂ by intercalation of Li-ions, which is then followed by an irreversible conversion reaction at 200–600 mAh/g resulting in Sn and Li₂S [27]. The subsequent lithiation/delithiation continues by the reversible alloying of lithium and tin at capacities beyond 600 mAh/g. The detailed lithiation reactions can be found in Supplementary Information, Equations (S1)–(S3). Up to now, no thermal and calorimetric analyses have been performed on SnS₂-based electrodes and/or electrode materials that have been subjected to electrochemical lithiation. However, to understand the nature and heat evolution of the reactions that occur with increasing temperature on the electrode level, differential scanning calorimetry (DSC) must be performed [25,28–31] along with a comprehensive physio-chemical characterization of the surface, near-surface, and bulk states of the electrode materials as a function of lithium content. Therefore, in this work, the DSC technique was used to investigate the thermal stability of SnS₂ anodes produced with a water-based slurry (CMC/SBR binder) as a function of capacity for the first time. This is supplemented by X-ray diffraction (XRD) analysis and X-ray photoelectron spectroscopy (XPS) analysis to correlate the crystalline phases present in the anodes and the surface species with the thermal behavior of the electrodes.

2. Materials and Methods

All materials used in this study are listed in Table 1. Commercially available SnS₂ was selected as the active material (AM) and all electrodes were subjected to aqueous processing using a 1:1 mixture of carboxymethyl cellulose (CMC) and styrene–butadiene rubber (SBR) as the binder system with carbon black as the conductive additive. In the first step, the SnS₂, carbon black, and CMC solution were combined in an 80/10/5 mass ratio of the solid components using a high-energy Turbo Stirrer (T 18 digital ULTRA-TURRAX®, IKA, Staufen, Germany) operating between 10,000 and 15,000 rpm. SBR was subsequently incorporated into the mixture to achieve an 80/10/5/5 final mass ratio of the solid components and then stirred at a lower speed of 3000 to 5000 rpm. This step at lower speed is required due to the susceptibility of SBR to damage and breaking. The resultant slurry was blade-coated onto a copper foil with a 250 µm gap size at a coating speed of 4 mm/s. The coated electrodes were initially dried at 80 °C for 12 h under vacuum. After punching the electrodes into discs using a 15 mm diameter die, they were subjected to further drying at 120 °C for 12 h in a vacuum, before being introduced into the glovebox without any contact to air. The final electrodes exhibited an average loading of 10.46 mg/cm², which corresponds to a theoretical areal capacity of 6.5 mAh/cm² assuming a theoretical reversible capacity of 623 mAh/g.

Scanning electron microscopy of the pristine electrodes was performed to gain insights into the surface condition and morphology of the pristine anodes. The imaging was performed on a Carl Zeiss Supra 40 (Carl Zeiss GmbH, Oberkochen, Germany) scanning electron microscope with Everhart–Thornley (ETD) and Through-Lens (TLD) detectors with a primary electron-beam energy of 2 keV.

For coin cell assembly of the type CR2032 (X2Lab, Singapore, Singapore), two different types of separators were used: two glass-fiber (Whatman GF/D, Celgard LLC, Charlotte, NC, USA) separators, each with a thickness of 0.25 mm, and a polymer-type separator

(Celgard, Celgard LLC, Charlotte, NC, USA). The polymer separator was placed in contact with the SnS_2 electrode to enable easier separation of the electrode from the separators after cycling for the DSC analysis and post mortem characterization. Lithium metal chips (15 mm disks, 250 μm thickness, PI-KEM, Tamworth, Staffordshire, UK) were used as counter electrodes. For the electrolyte, 120 μL of 1M LiPF_6 in ethylene carbonate: diethylene carbonate (EC: DEC) containing a 10% fluoroethylene carbonate (FEC) additive was used. The choice of this electrolyte was motivated by the ability of FEC to form LiF-rich, and mechanically robust SEI layers. This mitigates the continuous decomposition of the electrolyte during cycling, which can lead to the formation of an unstable SEI. A more stable SEI not only improves electrochemical cycling but should also have a positive impact on thermal stability, since the SEI is usually the first component to decompose exothermically during heating in DSC measurements. The coin cells were cycled at room temperature using a battery cycler (Arbin BT-21084, Arbin Instruments, Munich, Germany). In the first formation cycle, the specific current was set to 20 mA/g for generation of the Solid Electrolyte Interphase (SEI). For subsequent cycles, a specific current of 100 mA/g was adopted. Cycling was performed in the potential window between 1.2 V vs. Li^+/Li and 10 mV vs. Li^+/Li , and one constant current constant voltage (CC-CV) step was incorporated per cycle. After 10 cycles, the measurements were stopped at various States of Charge (SOCs), corresponding to specific capacities of 0, 100, 200, 300, 400, 500, and \sim 550 mAh/g. This cycling protocol ensures that the initial irreversible conversion of SnS_2 to Sn and Li_2S was complete, and that the electrodes achieved stable cycling performance and reproducible capacities before continuing further investigations.

Table 1. Details and characteristics of materials used for electrode processing.

Material	Brand Name	Company	State
Tin(IV)Sulfide	MKN-SnS2-900	mkNANO, Missisauga, ON, Canada	Powder (APS: 3 μm , hexagonal flakes)
Carboxymethyl cellulose	TEXTURECEL™ 2000 PA 07	IFF, Maastricht, Netherlands	Powder dissolved in H_2O
Styrene–butadiene rubber	SBR TRD104A	JSR Corporation, Tokyo, Japan	40 wt.% emulsion
Carbon black	C-NERGY™ SUPER C45	Imerys, Paris, France	Powder

After cycling, the cells were opened under argon atmosphere in an oxygen and humidity-controlled (<0.1 ppm of H_2O and <0.1 ppm of O_2) glovebox (MBRAUN, Garching, Germany). The electrodes were extracted and washed with dimethyl carbonate (DMC) for one minute. This washing step was performed to remove any weakly adhered residual electrolyte salts and additives. After washing, the electrodes were not subjected to additional drying steps. Instead, they were left inside the glovebox to allow the solvent to evaporate prior to further analysis. The electrode material was then carefully scraped from the current copper collector using a ceramic blade and transferred to a flat specimen alumina crucible with a lid. The masses of the extracted electrode materials are shown in Table S1. The DSC experiments were performed on the electrode material and not the electrodes in order to have improved thermal contact between the bulk electrode material and the bottom of the crucible. The crucible was then shuttled under argon to the DSC. All DSC experiments were carried out on a DSC 404 F1 Pegasus (Netzsch, Selb, Germany) under argon flow of 20 mL/min and a heating rate of 5 °C/min. The selected temperature range was from 25 °C (room temperature) to 350 °C. This temperature range was chosen to investigate the thermal behavior of SnS_2 at temperatures where decomposition of cathode active materials

has not yet started. According to literature, decomposition of typical cathode materials starts between 150 °C and 300 °C, depending on their state-of-charge [32]. The experiments were conducted twice for repeatability. The general experiment flow is visualized in Figure 2. Prior to the DSC measurements, temperature and sensitivity calibration were performed by measuring the melting points and melting enthalpies of pure indium, tin, and aluminum using the same measurement conditions as adopted for the electrodes. The sensitivity calibration allows for conversion of the DSC signal from μV to mW. The heat flow in mW was then divided by the sample's mass in mg to have a heat flow value in W/g and was then plotted versus temperature in °C. To obtain the heat energy released or absorbed in Joules per gram of the electrodes (J/g), an integration of the area of interest under the curve was performed to obtain a value in W.K/g. Knowing the heating rate (5 K/min), this can be converted to W.s/g which is equal to J/g. The integration limits are shown exemplary in Figure S1a for the fully discharged and Figure S1b for the fully charged electrode. The area under the curve for the SEI is labeled as I in Figure S1 and the binder reaction is labeled as II. The total heat effect of the electrode would be the sum of these values. For the fully charged electrode, area T is the area associated with the heat effect of the melting of tin. Since there were two DSC measurements per SOC, the values for the heat effects were averaged. The errors were calculated using the standard error of the mean. Additionally, prior to the measurements, a measurement with an empty crucible was performed for baseline correction. It showed a straight line and was therefore not included in the evaluations, since it would not change the results of integration.

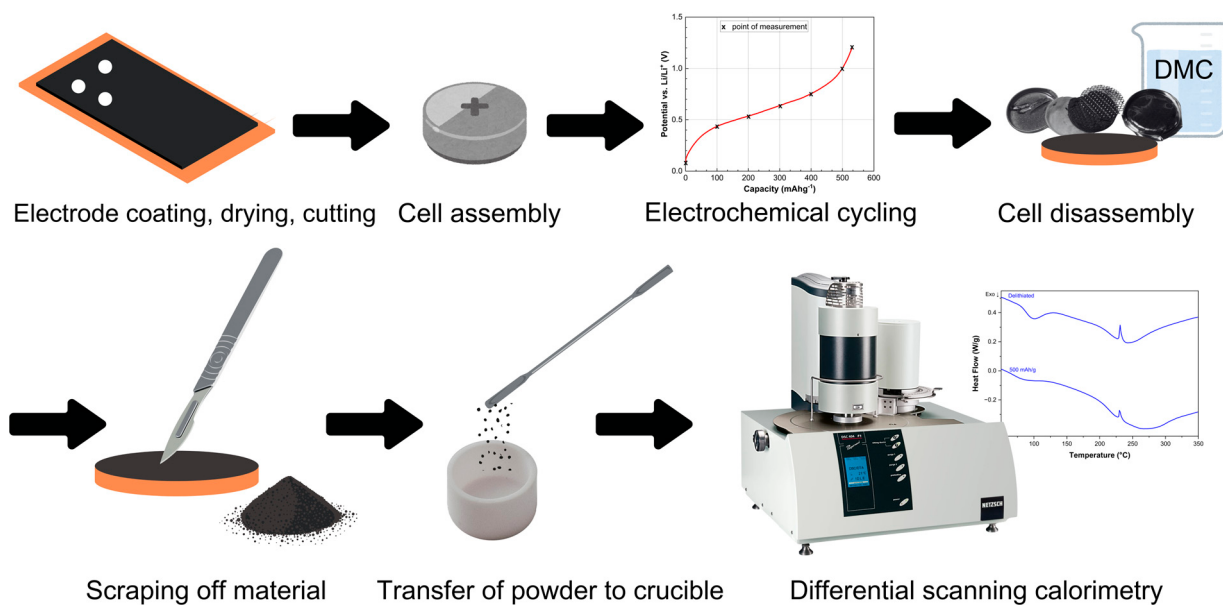


Figure 2. Schematic illustration of the experiments' setup.

After cycling, post mortem X-ray diffraction (XRD) and X-ray photoelectron spectroscopy (XPS) were performed on the electrodes to gain further insights into the bulk composition and surface chemistry of the electrode material before the DSC analysis. For the XRD measurements, the washed electrodes were cut and fixed on a monocrystal silicon sample holder using a double-sided tape inside an Ar-filled glove box. The sample holder was then sealed tightly with a polycarbonate dome to maintain an air-free environment during the analysis. The XRD measurements were conducted using a Bruker D8 Advance (Bruker AXS, Karlsruhe, Germany) diffractometer (θ/θ -geometry) with a Cu-K α radiation source (40 kV/40 mA) and an energy dispersive Lynxeye2 detector. Topas software[®] (Version V7) was used to evaluate the obtained patterns from XRD analysis based on full-profile

Rietveld-refinements. X-ray photoelectron spectroscopy (XPS) was used to analyze the presence of tin, sulfur, carbon, oxygen, nitrogen, sodium, phosphorus, fluorine, and lithium, as well as acquiring each electrode's valence band spectra (VBS) using a Nexsa™ Surface Analysis System (Thermo Scientific, Schwerte, Germany) equipped with an Al-K α radiation source operating at 72 W and a pass energy of 200 eV. With a measurement spot size of 400 μm and an energy step size of 0.1 eV for the survey spectrum, spectra acquisition was set to a threshold of 10 passes at a pass energy of 50 eV. For data analysis, CasaXPS software (version 2.3.25PR1.0) was utilized, applying a mixed peak fitting model combining Gaussian and Lorentzian components (GL(30)).

3. Results

The scanning electron microscopy (SEM) images of the pristine electrodes, shown in Figure 3, indicate an even distribution of tin (IV)sulfide particles (gray platelets) and carbon black. The SnS₂ platelets are homogenously embedded in a dense network of carbon black and binder (Figure 3a), and the platelets are crack-free (Figure 3b).

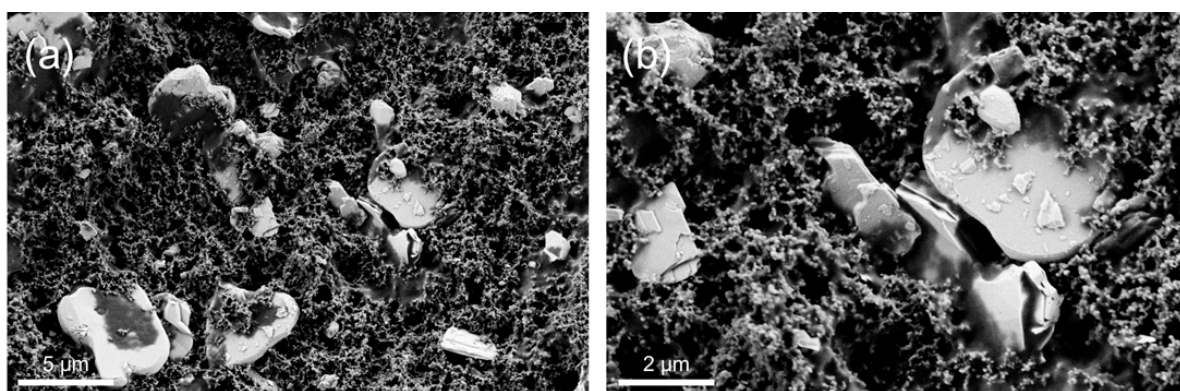


Figure 3. SEM images of pristine electrodes at (a) 10 k and (b) 25 k-times magnification.

Figure 4a shows the measured voltage profile of the SnS₂-electrodes as a function of specific capacity during the formation and first lithiation and delithiation cycles. The figure shows 3 plateaus: 0 to ~200 mAh/g corresponding Li $^+$ intercalation into SnS₂ to form Li_xSnS₂; ~200 to ~600 mAh/g corresponding to the irreversible conversion of Li_xSnS₂ to Sn and Li₂S; and above ~600 mAh/g the reversible alloying of Sn with Li to form Li-Sn alloys. In the formation cycle, the theoretical value of 1209 mAh/g for full lithiation of SnS₂ to Li₁₇Sn₄ is attained. This theoretical value arises from the two-step lithiation pathway of SnS₂. First, Li $^+$ intercalation and subsequent (irreversible) conversion to Sn and Li₂S consume 4 mol Li $^+$ per mol SnS₂, corresponding to 586 mAh/g. The metallic Sn produced then undergoes a reversible alloying reaction with an additional 4.25 mol Li $^+$ (623 mAh/g), forming Li₁₇Sn₄. In total, 8.25 mol Li $^+$ can be accommodated per formula unit of SnS₂, which corresponds to a full-lithiation capacity of 1209 mAh/g. However, when charging is performed up to a cut-off potential of 1.3 V vs. Li $^+$ /Li, a capacity of 550 mAh/g is obtained. This corresponds to a practical first-cycle coulombic efficiency of 45.5% (theoretical value: 51.5%), which is mainly attributed to the irreversible loss of electroactive lithium due to the formation of inactive Li₂S. However, the remaining cycles show stable performance and coulombic efficiencies of 99.5–100%, based on the maximum reversible capacity of 550 mAh/g, which is associated with the fully delithiated, i.e., fully charged state of the active component of the electrodes.

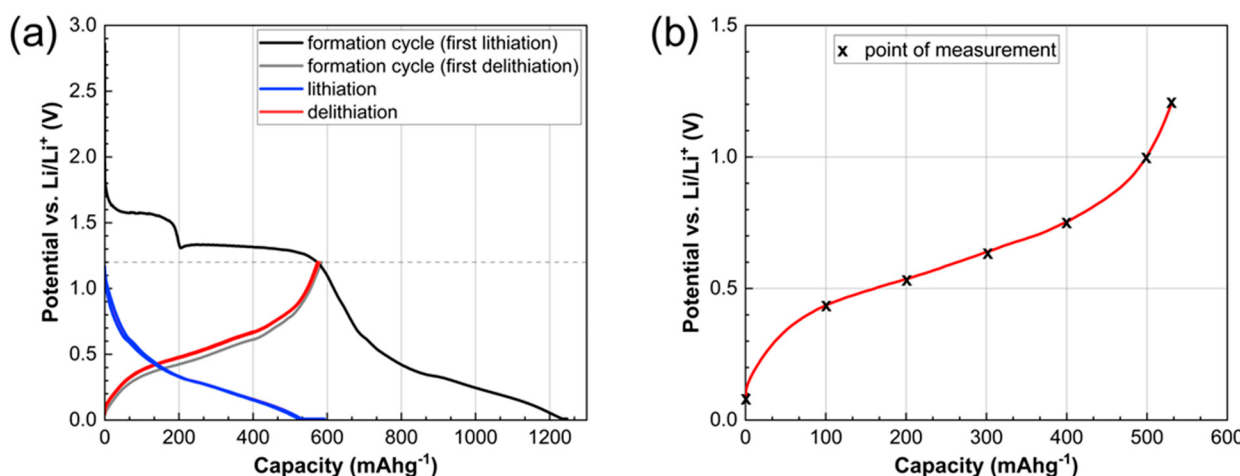


Figure 4. (a) Capacity curve and voltage profile of $\text{SnS}_2/\text{carbon}/\text{CMC:SBR}$ anodes and (b) points of interest in the 11th cycle of the SnS_2 anode (0–100–200–300–400–500–max. mAh/g).

The electrodes were charged to six different SOCs for the further investigations. The selected specific charge capacities are: 100, 200, 300, 400, 500 and 550 mAh/g. The electrodes obtained at a specific charge capacity of 550 mAh/g are considered fully charged (100% SOC), as this capacity corresponds to the largest amount of lithium which can be reversibly extracted from the electrodes. The electrodes obtained at specific capacities between 100 and 500 mAh/g are partially charged. In addition, a seventh electrode was selected for investigation. This electrode was obtained after full discharge (0% SOC). It contains the maximum amount of lithium and is assigned a specific charge capacity of 0 mAh/g as no lithium was extracted. To obtain sufficient electrodes and electrode material associated with each specific charge capacity investigated (Figure 4b), a minimum of three (3) coin cells were assembled, cycled, and stopped at the selected specific charge capacity.

The measured heat flow signals in W/g vs. temperature in $^{\circ}\text{C}$ obtained from the DSC investigations of the electrode materials at the selected states of charge are shown in Figure 5. Generally, for all samples investigated, the thermal decomposition starts at approximately $50\text{ }^{\circ}\text{C}$ with a maximum exothermic effect between $\sim 80\text{ }^{\circ}\text{C}$ and $\sim 90\text{ }^{\circ}\text{C}$, which may be correlated with the decomposition of the SEI on anode materials [33]. Additionally, a second broad exothermic peak with a minimum around $245\text{--}265\text{ }^{\circ}\text{C}$ was observed. More specifically, the SnS_2 -based electrodes that are fully discharged and the electrodes delithiated up to 300 mAh/g show (Figure 5a) similar thermal decomposition behaviors, where the decomposition begins exothermically with the SEI followed by the second broad exothermic peak between 245 and $265\text{ }^{\circ}\text{C}$. The 400 mAh/g electrode, however, shows in addition to the SEI and binder peaks a very small endothermic peak at $\sim 229\text{ }^{\circ}\text{C}$; see Figure 5b. This small peak is correlated with the endothermic melting of tin. In both the electrodes cycled up to 500 mAh/g and the fully delithiated electrode (Figure 5b), the peak corresponding to the endothermic melting of tin becomes increasingly pronounced.

Figure 6 shows the DSC results of the same, fully lithiated electrode material which was subjected to the heating program twice. Whereas the exothermic effects at $\sim 80\text{ }^{\circ}\text{C}$ and $\sim 265\text{ }^{\circ}\text{C}$ are visible in the first heating, they are absent when the same material is subjected to the second heating. This confirms that the thermal decomposition processes are completed in the first heating. To better understand the nature of the exothermic effect starting above $200\text{ }^{\circ}\text{C}$ in the electrodes and to isolate the thermal effects that stem from heating the electrode materials mixture, both CMC and the SBR were subjected to DSC measurements using the same heating program as for the electrode materials. In Figure 7a, the result for CMC is shown. The first broad endothermic peak starting at approx. $100\text{ }^{\circ}\text{C}$ is correlated with the loss of adsorbed water. The following two exothermic peaks with

onsets at 266 °C and 272 °C stem from the splitting of the functional groups alongside the decomposition of the cellulose chain followed by the cellulose chain's carbonization [34]. Therefore, it is very likely that the exothermic peak observed in the electrodes around 245–265 °C represents the decomposition of the Na-CMC binder. As for the SBR (Figure 7b), it is thermally stable in the chosen temperature range, which agrees with the literature, where it is reported to decompose above 350 °C [35].

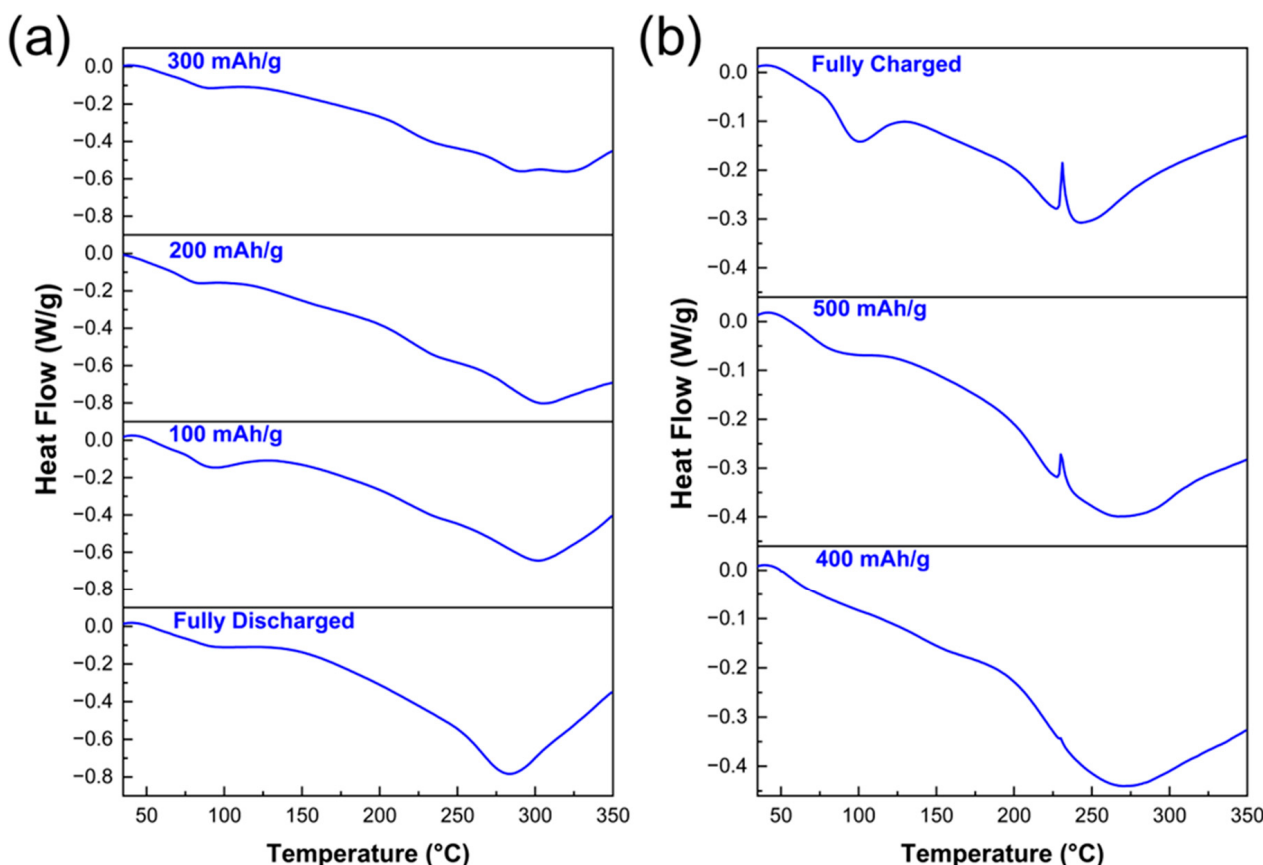


Figure 5. Seven DSC curves of SnS_2 electrodes cycled until (a) 0 (fully lithiated/discharged), 100, 200, and 300 mAh/g , (b) 400, 500 mAh/g and fully delithiated/charged.

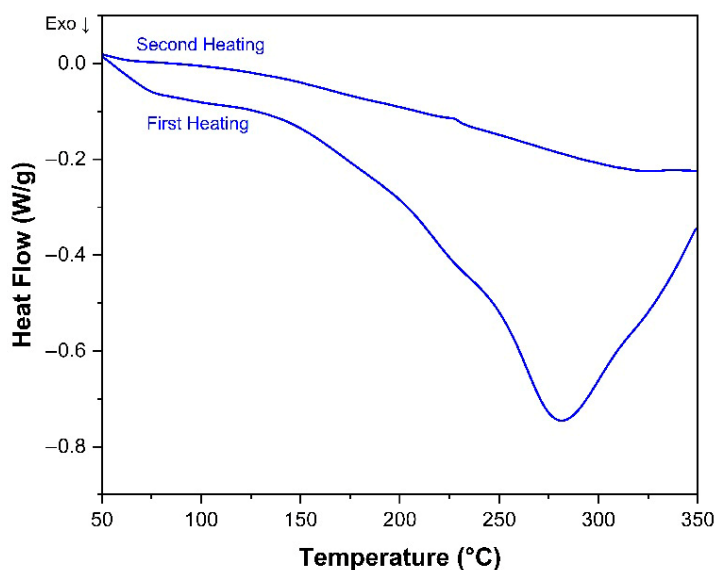


Figure 6. DSC curves of the same fully lithiated electrode heated twice.

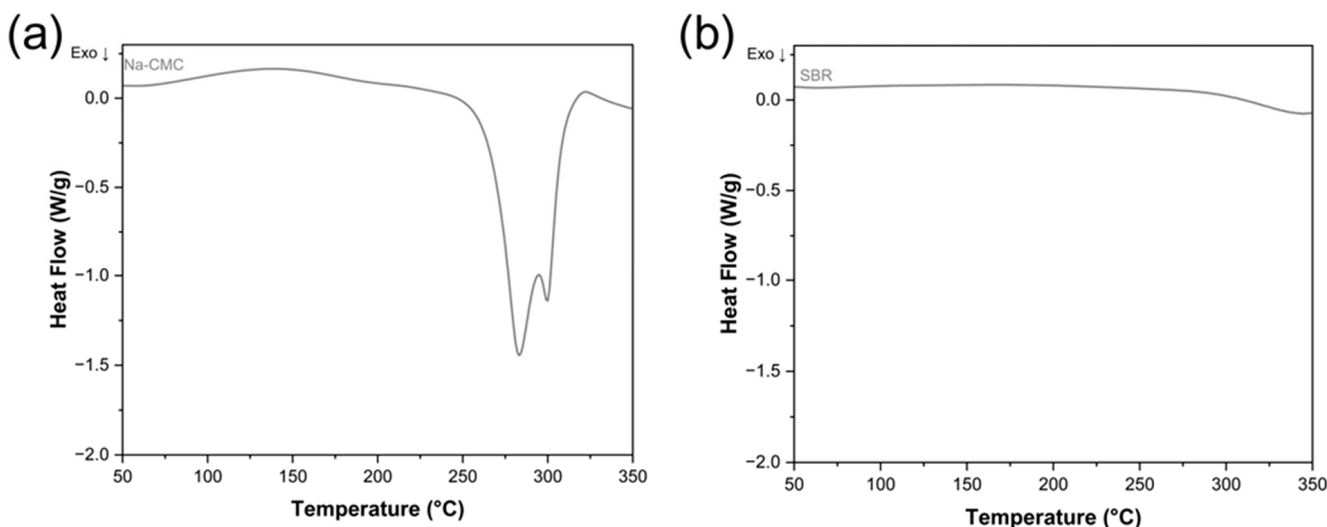


Figure 7. DSC graphs of (a) Na-CMC and (b) SBR.

The exothermic heat release associated with the decomposition of the SEI was quantified and is shown in Figure 8a. The heat energy released or absorbed in J/g for the electrodes was obtained by integrating the area of interest under the DSC curve (Heat flow vs. temperature), and applying the sensitivity calibration to convert the integrated signal from $\mu\text{V}/\text{mg}$ to J/g, using the formula:

$$\Delta H \left(\frac{\text{J}}{\text{g}} \right) = \frac{A \cdot (\mu\text{V} \cdot \text{K}) \cdot C \left(\text{J} \cdot \mu\text{V}^{-1} \cdot \text{s}^{-1} \right)}{\alpha (\text{K} \cdot \text{s}^{-1}) \cdot m(\text{g})}$$

where A is the area under the DSC curve, C is the sensitivity calibration constant, α is the heating rate and m is the mass of the active material in the electrode. Example integration limits are shown in Figure S1a for the fully discharged and Figure S1b for the fully charged electrode to show all areas of interest (SEI, Sn, and binder reaction). The SEI decomposition energy of the electrodes lies between $-13 \text{ J/g} \pm 4$ and $-42 \pm 4 \text{ J/g}$. However, no consistent trend was observed in the SEI decomposition heat evolved as a function of state of charge of the electrodes. This observation is discussed in more detail below; see chapter 4. To compare the endothermic effect of tin melting observed in the DSC experiments of electrodes at 400 mAh/g, 500 mAh/g, and fully charged, the area under the curve was integrated leading to a number corresponding to the heat effect (enthalpy) in J/g. This was then plotted and can be seen in Figure 8b. The endothermic effect for the melting of tin increases with delithiation: $\sim 0.2 \pm 1 \text{ J/g}$ for the 400 mAh/g, $\sim 2.5 \pm 1 \text{ J/g}$ for the 500 mAh/g, and $\sim 4.0 \pm 1 \text{ J/g}$ for the fully delithiated electrode. The highest endothermic contribution is consequently in the fully delithiated electrode which should contain the highest amount of Sn. When all exothermic and endothermic contributions in the electrodes are considered, a clear trend can be established in Figure 8c. The total energy generated decreases with delithiation even when taking the standard error of the mean into account ($\pm 29 \text{ J/g}$). The fully lithiated electrode generated in total $-325 \pm 29 \text{ J/g}$, on the other hand, the electrodes delithiated up to 500 mAh/g and fully delithiated generated the least amount of heat ($-150 \pm 29 \text{ J/g}$ and $-140 \pm 29 \text{ J/g}$). The trend of increasing exothermic behavior of electrodes on heating at higher lithiation levels was also observed in the literature [36–39] where the delithiated graphite electrodes generate less heat compared to lithiated graphite electrodes.

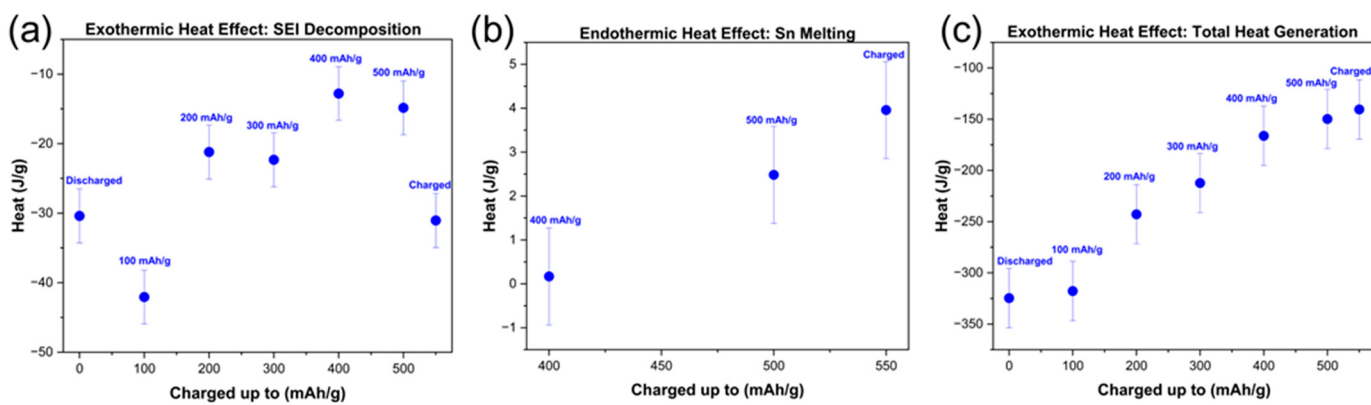


Figure 8. (a) Exothermic heat effect of SEI of SnS_2 electrodes, (b) endothermic heat effect of Sn melting, (c) total heat effect of electrodes.

A summary of the average values of the heat effects is shown in Table 2.

Table 2. Average values of Exothermic SEI Effect, Endothermic melting of tin effect, and total heat effect of the electrodes.

Electrode Charged Until (mAh/g)	Exothermic SEI Effect (J/g)	Endothermic Sn Effect (J/g)	Total Exothermic Effect (J/g)
0	-30 ± 4	not observed	-325 ± 29
100	-42 ± 4	not observed	-310 ± 29
200	-21 ± 4	not observed	-243 ± 29
300	-22 ± 4	not observed	-213 ± 29
400	-13 ± 4	0.2 ± 1	-166 ± 29
500	-15 ± 4	2.5 ± 1	-150 ± 29
550	-31 ± 4	4.0 ± 1	-140 ± 29

In order to correlate the thermal stabilities of the electrodes with the bulk and surface states of the electrodes, both XRD and XPS were performed. The phases identified by XRD are shown in Table 3, and the respective XRD patterns are shown in Figure S2. The patterns were subjected to a full-profile Rietveld refinement. The copper phase detected in the XRD patterns of the electrodes at 0, 100, 300 and 550 mAh/g originates from the copper current collector on which the electrodes were coated. The absence of Cu-peaks in the XRD patterns of electrodes at 200, 400, and 500 mAh/g may be caused by the lack of penetration of the radiation source for those samples in the measurement configuration. The two wide peaks at approx. $2\theta = 19^\circ$ and 26° come from the protection dome and the double-sided tape, respectively. Although several Li-Sn intermetallic phases may be expected to form, they are difficult to characterize with XRD since the phases evolved by electrochemical lithiation are often amorphous or nano-crystalline [40] resulting in rather weak and diffuse peaks with a high and noisy background. However, $\text{Li}_{17}\text{Sn}_4$ was confirmed in the electrode at 0 mAh/g, confirming that full lithiation could have taken place.

According to the XRD measurements, Sn was observed in all electrodes between 550 and 200 mAh/g, not only in the fully delithiated electrode at 550 mAh/g. In our experiments, the electrodes were delithiated to the indicated specific capacities, and the measured potentials correspond to the Li-concentration at the particle/electrolyte interface during delithiation. Delithiation starts when Li is extracted from the surface of the particles, and the resulting concentration gradient between surface and bulk can drive the diffusion of Li from the bulk to the surface. Since Sn was already detected in the electrodes at

200 mAh/g, but the measured potential corresponds to a higher concentration of Li at the surface, it may mean that the flux of Li from the bulk to the surface is sufficiently fast to result in the formation of Sn-rich regions within the particles. As the state of delithiation increases, the Sn-rich regions grow, enabling their easier identification at higher states of charge.

Table 3. Charge state of the electrodes and the phases found by XRD.

Electrode Charged Until (mAh/g)	Phases Found in XRD
0	Cu, Li ₁₇ Sn ₄
100	Cu
200	Sn, Cu
300	Sn, Cu
400	Sn
500	Sn
550	Sn, Cu

The XPS C1s spectra, Figure 9a, are similar across all seven electrodes. A pronounced peak at 285 eV confirms that C-H and C-C bonds are the main contributors [41]. In addition, minor peaks appear at 286.5 eV, likely due to C-O bonds or sp³-hybridized carbon, and at 283.2 eV, which can be assigned to sp¹-hybridized carbon atoms [42]. Moreover, a broad, flat region around 289 eV suggests the presence of carbonates and their decomposition products originating from electrolyte solvents (such as EC and DEC). This feature is usually absent from pristine uncycled electrodes [43].

The F1s scan shown in Figure 9a has its most prominent peak at 685.7 eV, which is attributed to metal fluorides—specifically LiF [41]. A less intense peak at 686.7 eV is assigned to residual LiPF₆ electrolyte salt [44]. While previous reports indicate that decomposition products of LiPF₆ can shift the binding energy to 687 or even 688 eV [41], such a shift is not observed in this study. Since the F1s scan remains consistent across all stages of lithiation, it is suggested that LiF formation is completed before the tenth cycle.

In the O1s scan, Figure 9a, the most prominent peak appears at 532 eV, which is attributed to C=O bonds in lithium alkyl carbonates (R-O-CO₂-Li) and lithium carbonates (Li₂CO₃) [44]. These compounds are typical for the SEI layer. A second peak at around 533.5 eV indicates the presence of C-O species, likely originating from the C-O-C groups in the CMC binder [45]. Additionally, small contributions at a low binding energy of 529 eV suggest the formation of metal oxides such as SnO₂ or SnO, eventually causing a shift toward lower binding energies [46].

Regarding the P2p electrons, Figure 9b, the most prominent peak in the lithiated state is observed at 134.0 eV and is attributed to electrolyte decomposition products such as Li_xPO_yF_z [47]. However, as the state of delithiation increases, this peak decreases in intensity. In contrast, the peak at higher binding energies, specifically at 137.3 eV, is assigned to Li_xPF_y [48]. At 0 mAh/g, this higher-energy peak appears as a small, predominantly isolated feature, but as the state of the electrodes progresses toward fully delithiated, it broadens and increases in intensity relative to the 134 eV peak. During lithiation (at potentials below 1 V vs. Li/Li⁺), the electrolyte can degrade, resulting in higher intensities of the peaks associated with electrolyte decomposition products. However, as the state of delithiation increases, the relative intensities of these two peaks change. Therefore, what may first appear to be an increase in Li_xPF_y could also indicate the formation of a new species. Sn4s is known to appear at 137.1 eV [49], and since metallic Sn is forming with progressing delithiation, this may explain the relative increase in the peak at ~137 compared to the one at 134 eV.

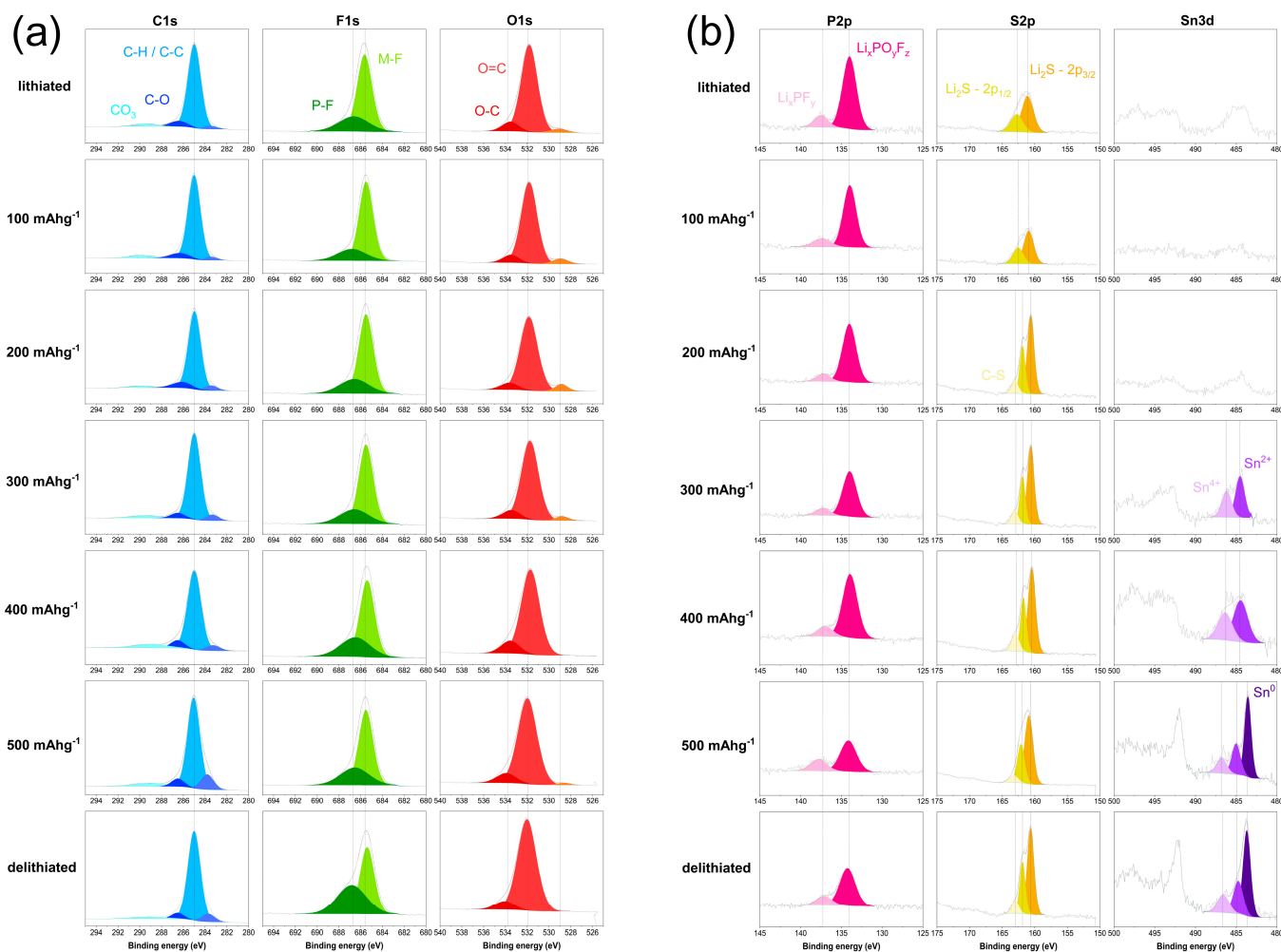


Figure 9. XPS scans of (a) C1s, F1s and O1s and (b) P2p, S2p and Sn3d of cycled anodes in fully lithiated state, at 100, 200, 300, 400, 500 mAh/g and fully delithiated.

In the lithiated state, as well as when charged to 100 mAh/g, the S2p scan, Figure 9b, shows a prominent peak at 161 eV and a smaller peak at 162.2 eV. These peaks correspond to the S2p_{3/2} and S2p_{1/2} electrons of Li₂S, respectively [50,51]. In samples that were more delithiated, these peaks are slightly shifted to 160.6 eV and 161.9 eV, respectively [52]. These shifts of 0.4–0.3 eV are not significant and could be attributed to several factors, such as changes in the oxidation state of sulfur during the formation of polysulfides (e.g., Li₂S₂), therefore reduced lithium coordination, and altered electronic screening, all of which can be caused with advanced state of delithiation [53]. Lastly, a shoulder at 163.1 eV is assigned to C-S bonding [52] likely resulting from side reactions of Li₂S with carbon-containing species such as carbonates from the electrolyte. Finally, the Sn3d scan (Figure 9b) indicates that the formation of near-surface tin-species begins at a capacity of 300 mAh/g, at a potential of approx. 0.6 V vs. Li⁺/Li. Measurements at 0, 100, and 200 mAh/g display mainly background noise and no clear peak. According to the literature, the peaks for Sn shift to lower binding energies with decreasing oxidation state [54]. At 300 and 400 mAh/g, we can observe peaks at 486.2 eV and 484.6 eV, indicating Sn species at higher oxidation states, such as 4+ and 2+, respectively (Sn3d 5/2) [55]. With further delithiation up to approximately 500 mAh/g or up until fully delithiated state, another sharp peak at even lower binding energies of 483.6 eV arises, which is due to the presence of metallic Sn [56]. The formation of Sn⁰ species furthermore causes a small shift in the Sn⁴⁺ and Sn²⁺ peaks of +0.5 eV each. These findings align with our observations mentioned earlier in the discussion of the O1s scans. The peak at 529 eV, indicating metal oxides, decreases and finally disappears, as the

higher binding energy peaks in the Sn3d scans decrease simultaneously. This suggests that Sn in tin oxides (SnO , SnO_2) gets reduced with increased state of delithiation. However, the remaining species of SnO_x appear to have stronger binding energies, hence the shift of +0.5 eV. Band structure effects can cause energy shifts, which are not due to change in oxidation state, therefore causing Sn^{2+} and Sn^{4+} peak shifting during Sn^0 formation [57].

In the valence band spectra (VBS), Figure 10, similar features are observed across the lithiated states corresponding to 100, 200, 300, and 400 mAh/g. The most intense peak at the highest binding energy, located around 30 eV, is attributed to the F2s electrons from electrolyte-derived fluorine species [58]. At 24.0 eV, a prominent peak corresponding to the Sn4d electrons is observed [59]. Additional smaller peaks appear at 19.8 eV (O2s from the binding agents, carbonates and environmental moisture), 17.0 eV (P3s from LiPF_6), 13.6 eV (P3p from LiPF_6), 9.6 eV (F2p from LiPF_6), and 5.8 eV (C2p from the binding agents and carbonates), which are consistent with components from the electrolyte [60] and binder system [61].

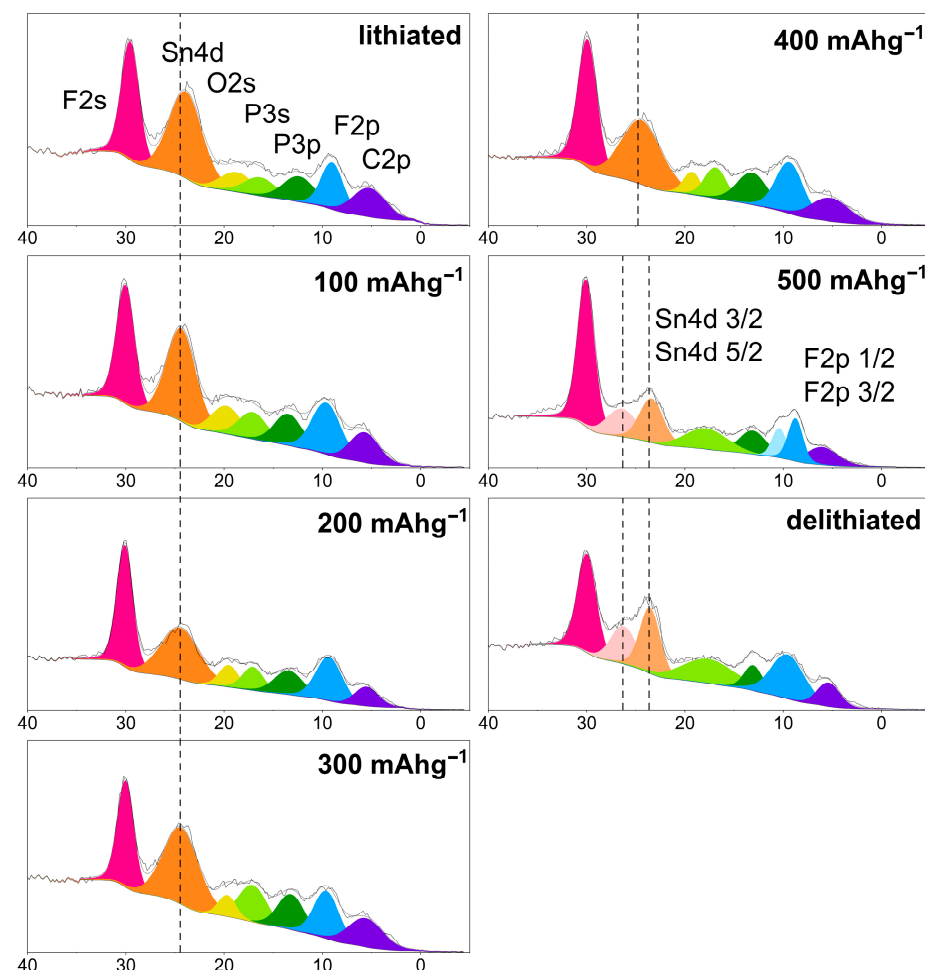


Figure 10. XPS-VBS scans of cycled anodes in fully lithiated state, at 100, 200, 300, 400, 500 mAh/g and fully delithiated.

Notably, after reaching 500 mAh/g, the Sn4d peak splits into two distinct features at 26.6 and 23.6 eV, respectively. This may correspond to the spin-orbit splitting of the Sn4d orbital into the 3/2 and 5/2 components, which aligns with the small doublet separation of 1–2 eV [62]. The initial single broad peak at approximately 24 eV likely reflects Sn in a chemically mixed or disordered environment, such as in electrochemically insulated SnS_2 [61] (Sn^{4+}) [63] or other species, such as SnF_4 (Sn^{4+}) or SnF_2 (Sn^{2+}) [43]. Upon delithiation, the observed splitting suggests that Sn atoms now occupy multiple, chemically

distinct environments. These may include metallic Sn^0 , and intermediate reduced states formed during the reduction of Sn^{4+} and Sn^{2+} to Sn^0 . Metallic tin, in particular, is known to exhibit a sharper and more well-defined 4d spin-orbit doublet compared to Sn in compound phases.

The O2s and P3s peaks appear to broaden and merge into a single, unresolved feature. This may reflect changes in the chemical environment associated with the decomposition of organic carbonate solvents (such as EC, DEC, or FEC), contributing to the O2s signal, and the formation of surface species such as $\text{Li}_x\text{PF}_y\text{O}_z$, which contributes to the P3s peak [64]. Such evolution is consistent with solid electrolyte interphase (SEI) growth and increasing chemical complexity.

A further key observation is the emergence of a doublet at 10.4 and 8.8 eV, which is assigned to spin-orbit splitting of the F2p level into the 1/2 and 3/2 components. This splitting indicates the presence of highly ionic fluorine environments, likely corresponding to LiF formed via the decomposition of LiPF₆ or reduction of FEC [60,65]. Importantly, this sharp splitting is only observed in electrodes that were cycled to 500 mAh/g. Lastly, throughout the spectra, other F- and C-related peaks remain largely unchanged, indicating that the main electronic and chemical changes are associated with the evolution of Sn-containing species and the formation of inorganic SEI components.

4. Discussion

According to the measurements performed, it can be observed that when SnS₂-based electrode materials at different states of delithiation are heated, the first reaction that takes place is the exothermic decomposition of the SEI. At a heating rate of 5 °C/min, the peak for this reaction occurs between 86 and 99 °C. This temperature range is consistent with the thermal decomposition of the SEI on other anode materials, where the temperatures reported in the literature lie between 80 °C and 120 °C [33,66]. According to literature, the SEI may be considered as a bilayer consisting of a mostly inorganic inner compact layer that is in contact with the electrode (with components such as LiF, Li₂CO₃, and Li₂O) and a mostly organic outer layer in contact with the electrolyte (with components such as lithium alkyl carbonates, lithium alkoxide, and lithium oligomer) [67]. The characteristic onset and peak maximum temperatures as well as the heat released are influenced by the chemistry of SEI formation, which are in turn determined by the choice of electrolyte salt [68], electrolyte additive [69], and the organic solvent [70]. In the SEI's thermal decomposition reaction, the less stable inorganic and the organic components of the SEI, such as the lithium alkyl carbonates, lithium ethylene decarbonate, $\text{Li}_x\text{PO}_y\text{F}_z$ which are observed to be present on the SnS₂ electrodes (according to the XPS analysis), decompose into more stable SEI species such as lithium fluoride or lithium carbonate [71–73]. An example for the thermal decomposition reaction of an organic component of the SEI is $(\text{CH}_2\text{OCO}_2\text{Li})_2 \rightarrow \text{Li}_2\text{CO}_3 + \text{C}_2\text{H}_4 + \text{CO}_2 + 0.5 \text{O}_2$ [74]. Another possible decomposition reaction could stem from LiPF₆, which is still present on the electrodes according to the XPS analysis. LiPF₆ is thermally stable in a dry inert environment up to 107 °C and decomposes into LiF as a solid product and PF₅ as a gaseous product at 107 °C. However, when moisture is present, a reaction occurs at around 87 °C causing PF₅ to further decompose into POF₃, and HF [73]. Nevertheless, this moisture decomposition is not expected to happen, since the electrodes were handled in a moisture-free Argon flow in the DSC. In any case, PF₅ is a strong Lewis acid and its reaction with the SEI at high temperatures plays a significant role in the decomposition of the SEI, as the Li₂O and carbonate species are vulnerable to the PF₅ attack [75].

The SEI generally has a dynamic nature with changes in thickness according to the state of charge. Usually, the SEI is thicker when the electrode is lithiated compared to when

it is delithiated [76]. This change in SEI thickness could lead to a difference in the SEI's exothermic decomposition. Nonetheless, establishing a trend according to the decomposition of the SEI in the tested electrodes was complicated by the brief washing of the electrode with DMC. This was done to remove residual amounts of the electrolyte which can react exothermically with the electrodes [36] and increase the heat released [29]. However, the SEI itself is soluble in the DMC solvent, and any partial dissolution of the SEI during the washing step could impair the quantitative determination of the energies released [77,78]. Furthermore, the measured DSC signal heavily depends on the thermal contact of the electrode materials particles with the bottom of the crucible. A similar difficulty in establishing a trend of the energy released from the SEI according to the electrode's state of charge was observed in Wang et al. [36] for graphite electrodes. Regardless, the results show that the thermal decomposition reaction of the SEI is complete in the first heating cycle as there are no heat flow effects during the second heating of the fully lithiated electrode.

In this study, two trends according to the state-of-delithiation or state-of-charge, however, could be established. The first is the endothermic heat effect associated with the melting of metallic tin. From the fully delithiated electrode material at 550 mAh/g up to the partially delithiated electrode at 400 mAh/g, an endothermic peak corresponding to the melting of tin can be seen in the measured DSC heat flow signals. These peaks become sharper and more pronounced at higher states of delithiation with the sharpest peak observed in the fully delithiated electroactive material. Using Faraday's law in combination with the Li-Sn phase diagram [7], the theoretical lithium composition in the Li-Sn system due to the alloying reaction of lithium with Sn at 400 mAh/g and 500 mAh/g should be $\text{Li}_{1.5}\text{Sn}$ and $\text{Li}_{0.8}\text{Sn}$, respectively. These compositions correspond to the two-phase equilibria $\text{Li}_7\text{Sn}_3 + \text{LiSn}$ and $\text{LiSn} + \text{Li}_2\text{Sn}_5$, respectively. Under equilibrium conditions, these electrodes should not contain metallic tin. Nevertheless, as mentioned earlier, lithiation/delithiation is a bulk process that starts from the surface of the active material particles and continues into the bulk material by Li-ion diffusion. This leads to the detection of Sn in the XRD of several electrodes, even at 200 mAh/g, the identification of metallic tin in the XPS evaluation for the fully delithiated sample at 550 mAh/g as well as in the sample at 500 mAh/g, and the appearance of the melting peak for Sn in the measured heat flow signals of the samples charged to 400 mAh/g and higher. Our results show that XRD with Rietveld analysis is the most sensitive technique for identifying crystalline Sn in the electrode material, as Sn could already be observed in the electrodes delithiated to 200 mAh/g. Therefore, the threshold of Sn-detection is much lower in the case of XRD (1–2 mass% of Sn). On the other hand, amorphous Sn could be detected via DSC. Additionally, the aforementioned random distribution of particles that are in contact with the bottom of the crucible could play a role here.

Even though the endothermic contribution of tin melting at 229 °C is quite small, it could be beneficial in the case of thermal runaway of lithium-ion batteries. The melting temperature of tin overlaps with the exothermic decomposition and oxygen release of many common cathode materials like NMC 811 ($\text{LiNi}_{0.8}\text{Mn}_{0.1}\text{Co}_{0.1}\text{O}_2$) at 212 °C [79], and NCA ($\text{LiNi}_x\text{Co}_y\text{Al}_z\text{O}_2$) at 240 °C [80]. This overlap of temperatures means that the endothermic nature of the melting of tin could lower the exothermic energy contribution from the cathode decomposition. In addition, Sn can act as a trap for the released oxygen forming thermodynamically stable SnO_2 .

The second established trend is related to the reduction of the total exothermic heat generated from the electrodes with increased delithiation which reduces even further when higher amounts of metallic tin are melted. This means that the electrode is the safest, in terms of exothermic energy release, at the lowest state of lithiation.

5. Conclusions

In this study, the thermal stability of SnS_2 -based electrodes was investigated for the first time. The DSC results revealed two general thermal events in all electrodes: two exothermic peaks, the first starting below 100 °C corresponding to the decomposition of the SEI and the second starting at 200 °C corresponding to the Na-CMC binder decomposition. Additionally, an endothermic peak associated with the melting of tin was observed from 400 mAh/g until full delithiation at >500 mAh/g. The heat generated from the decomposition of the SEI ranged from -13 J/g to -31 J/g and was correlated with the decomposition of many SEI species detected in the XPS. However, a clear trend between heat generated from the SEI decomposition and the state of delithiation of the electrodes could not be established. On the other hand, it was consistently observed that (i) the tin melting peak increases with increased delithiation, thereby confirming the presence of metallic tin in highly delithiated electrodes and (ii) the total heat generated from the electrodes decreased with increased delithiation, which was also observed for graphite electrodes in the literature.

Another interesting finding in the XRD results was the detection of crystalline tin as early as at 200 mAh/g, suggesting X-ray method-dependent detection thresholds (>1–2 mass%). According to the Li-Sn phase diagram, Sn should only be detected in the fully delithiated electrode. However, Sn was observed starting from electrodes delithiated up to 200 mAh/g. Since in XPS, Sn 3d- and Sn 4d-peaks (VBS) for metallic tin were only present only in the electrodes at 500 mAh/g and 550 mAh/g (fully delithiated), tin found at lower capacities should be located in the bulk phase. These observations indicate local Li concentration gradients and possibly different diffusion kinetics during charging and discharging, as is often observed.

The results presented in this paper suggest that a potential pathway to improve safety in future lithium-ion batteries could be the use of electrode materials that contain metallic elements which melt at lower temperatures and thus contribute endothermically to the heat balance. This could be overlapped with the exothermic effect of the thermal decomposition of the cathodes and oxygen release. Additionally, these metallic elements could act as a trap for the released oxygen from the cathode to form more thermodynamically stable metal oxides. Furthermore, the data presented here can be used for modeling the thermal behavior of SnS_2 -based batteries and designing future experiments that involve full cells and more battery components.

Supplementary Materials: The following supporting information can be downloaded at <https://www.mdpi.com/article/10.3390/batteries11100378/s1>, Table S1: Masses of the extracted electroactive materials. Figure S1: (a) Integration of the fully discharged electrode from the DSC, and (b) of the fully charged electrode. Figure S2: Voltage profile of SnS_2 anodes cycled for 10 times. Figure S3: XRD in the range of $2\Theta = 15\text{--}100^\circ$ of SnS_2 anodes cycled for 10 times.

Author Contributions: Conceptualization, H.F., D.M.C., J.K., Y.S. and M.R.; methodology, M.R. and J.K.; validation, H.F. and D.M.C.; investigation, M.R. and J.K.; resources D.M.C. and H.F.; data curation, J.K. and M.R.; writing—original draft preparation, J.K. and M.R.; writing—review and editing, D.M.C., H.F., Y.S., J.K. and M.R.; visualization, J.K. and M.R.; supervision, H.F., Y.S. and D.M.C.; project administration, D.M.C.; funding acquisition, D.M.C. and H.F. All authors have read and agreed to the published version of the manuscript.

Funding: This work was funded by the Austrian Research Promotion Agency (FFG) under grant number 891450 with project title “Modellierung und Entwicklung von Silizium-Zinnsulfid Kompositanoden für Lithium-Ion Batterien der Generation 3b” (MoSiLIB).

Data Availability Statement: Data are available on request.

Acknowledgments: Open Access Funding by the University of Vienna.

Conflicts of Interest: Authors Jana Kupka, Yuri Surace and Damian M. Cupid were employed by the company AIT Austrian Institute of Technology GmbH, which is a research and technology organization located in Austria. The remaining authors declare that the research was conducted in the absence of any commercial or financial relationships that could be construed as a potential conflict of interest.

Abbreviations

The following abbreviations are used in this manuscript:

DSC	Differential Scanning Calorimetry
LIB	Lithium-ion Battery
SEI	Solid Electrolyte Interphase
XRD	X-ray Diffraction
XPS	X-ray Photoelectron Spectroscopy
AM	Active Material
CMC	Carboxymethyl Cellulose
SBR	Styrene–Butadiene Rubber
ETD	Everhart–Thornley Detector
TLD	Through-Lens Detector
EC: DEC	Ethylene Carbonate: Di-Ethylene Carbonate
FEC	Fluoroethylene Carbonate
CCCV	Constant Current Constant Voltage
SOC	State of Charge
DMC	Dimethyl Carbonate
VBS	Valence Band Spectra
SEM	Scanning Electron Microscopy

References

1. Obrovac, M.N. Si-alloy negative electrodes for Li-ion batteries. *Curr. Opin. Electrochem.* **2018**, *9*, 8–17. [[CrossRef](#)]
2. Asenbauer, J.; Eisenmann, T.; Kuenzel, M.; Kazzazi, A.; Chen, Z.; Bresser, D. The success story of graphite as a lithium-ion anode material—fundamentals, remaining challenges, and recent developments including silicon (oxide) composites. *Sustain. Energy Fuels* **2020**, *4*, 5387–5416. [[CrossRef](#)]
3. Reichmann, T.L.; Gebert, C.; Cupid, D.M. Investigation of the Li solubility in the intermediate phase Li₁₇Sn₄ relevant to understanding lithiation mechanisms in Sn-based anode materials. *J. Alloys Compd.* **2017**, *714*, 593–602. [[CrossRef](#)]
4. Wang, C.; Yang, C.; Zheng, Z. Toward Practical High-Energy and High-Power Lithium Battery Anodes: Present and Future. *Adv. Sci.* **2022**, *9*, 2105213. [[CrossRef](#)]
5. Li, J.; Du, Z.; Ruther, R.E.; An, S.J.; David, L.A.; Hays, K.; Wood, M.; Phillip, N.D.; Sheng, Y.; Mao, C.; et al. Toward Low-Cost, High-Energy Density, and High-Power Density Lithium-Ion Batteries. *JOM* **2017**, *69*, 1484–1496. [[CrossRef](#)]
6. Nitta, N.; Yushin, G. High-capacity anode materials for lithium-ion batteries: Choice of elements and structures for active particles. Particle and Particle Systems Characterization. Part. Part. Syst. Charact. **2014**, *31*, 317–336. [[CrossRef](#)]
7. Li, D.; Fürtner, S.; Flandorfer, H.; Cupid, D. Thermodynamic assessment and experimental investigation of the Li-Sn system. *Calphad* **2014**, *47*, 181–195. [[CrossRef](#)]
8. Drüe, M.; Seyring, M.; Kozlov, A.; Song, X.; Schmid-Fetzer, R.; Rettenmayr, M. Thermodynamic stability of Li₂C₂ and LiC₆. *J. Alloys Compd.* **2013**, *575*, 403–407. [[CrossRef](#)]
9. Xin, F.; Whittingham, M.S. Challenges and Development of Tin-Based Anode with High Volumetric Capacity for Li-Ion Batteries. *Electrochem. Energy Rev.* **2020**, *3*, 643–655. [[CrossRef](#)]
10. Obrovac, M.N.; Chevrier, V.L. Alloy negative electrodes for Li-ion batteries. *Chem. Rev.* **2014**, *114*, 11444–11502. [[CrossRef](#)]
11. Glibo, A.; Eshraghi, N.; Surace, Y.; Mautner, A.; Flandorfer, H.; Cupid, D.M. Comparative study of electrochemical properties of SnS and SnS₂ as anode materials in lithium-ion batteries. *Electrochim. Acta* **2023**, *441*, 141725. [[CrossRef](#)]
12. Huang, Z.X.; Wang, Y.; Liu, B.; Kong, D.; Zhang, J.; Chen, T.; Yang, H.Y. Unlocking the potential of SnS₂: Transition metal catalyzed utilization of reversible conversion and alloying reactions. *Sci. Rep.* **2017**, *7*, 41015. [[CrossRef](#)]
13. Youn, D.H.; Stauffer, S.K.; Xiao, P.; Park, H.; Nam, Y.; Dolocan, A.; Henkelman, G.; Heller, A.; Mullins, C.B. Simple Synthesis of Nanocrystalline Tin Sulfide/N-Doped Reduced Graphene Oxide Composites as Lithium Ion Battery Anodes. *ACS Nano* **2016**, *10*, 10778–10788. [[CrossRef](#)]

14. Office of the European Union; Council of the European Union. Regulation (EU) 2024/1252 of the European Parliament and of the Council of 11 April 2024 Establishing a Framework for Ensuring a Secure and Sustainable Supply of Critical Raw Materials and Amending Regulations (EU) No 168/2013, (EU) 2018/858, (EU) 2018/1724 and (EU) 2019/1020 Text with EEA Relevance. 2024. Available online: <http://data.europa.eu/eli/reg/2024/1252/oj> (accessed on 4 June 2024).
15. Momma, K.; Izumi, F. VESTA: A three-dimensional visualization system for electronic and structural analysis. *J. Appl. Crystallogr.* **2008**, *41*, 653–658. [CrossRef]
16. Yoo, H.; Moon, J.H.; Seong, H.; Jin, Y.; Kim, G.; Jung, T.; Lee, J.B.; Kwon, S.-R.; Yang, M.; Choi, J. Enhanced reversible reaction of hexagonal SnS₂@rGO as anode materials for lithium-ion batteries: Analysis of the morphological change mechanism. *J. Energy Storage* **2024**, *96*, 112599. [CrossRef]
17. Yang, T.; Zhu, J.; Zhang, Y.; Zhang, Y.; Lin, R. Si/SnS₂ Nanocomposite for Lithium Ion Battery Anodes. *ACS Appl. Nano Mater.* **2023**, *6*, 22767–22773. [CrossRef]
18. Yang, R.; Liang, H.; Chen, M.; Lu, F. Entropy enhancement driven high initial Coulombic efficiency and capacity integrated SnS₂ nanosheets for lithium-ion batteries. *Electrochim. Acta* **2024**, *504*, 144932. [CrossRef]
19. Bekzhanov, A.; Daniyeva, N.; Jiang, Q.; Surace, Y.; Kleitz, F.; Cupid, D. Hydrothermally Synthesized SnS₂ Anode Materials with Selectively Tuned Crystallinity. *Small Sci.* **2024**, *5*, 2400516. [CrossRef] [PubMed]
20. Glibo, A.; Reda, M.; Surace, Y.; Cupid, D.M.; Flandorfer, H. Correlation between microstructure, thermodynamic stability, and electric work of tin sulfide active anode materials for Li-ion batteries. *J. Alloys Compd.* **2023**, *969*, 172320. [CrossRef]
21. Mukaibo, H.; Yoshizawa, A.; Momma, T.; Osaka, T. Particle size and performance of SnS₂ anodes for rechargeable lithium batteries. *J. Power Sources* **2003**, *119–121*, 60–63. [CrossRef]
22. Kong, X.; Wu, X.; Li, J.; Zhang, L.; Ouyang, H.; Feng, Q. One-Step Urothermal Synthesis of Li⁺-Intercalated SnS₂ Anodes with High Initial Coulombic Efficiency for Li-Ion Batteries. *ACS Appl. Nano Mater.* **2023**, *6*, 946–952. [CrossRef]
23. Cheng, Y.; Xie, H.; Zhou, L.; Shi, B.; Guo, L.; Huang, J. In-situ liquid-phase transformation of SnS₂/CNTs composite from SnO₂/CNTs for high performance lithium-ion battery anode. *Appl. Surf. Sci.* **2021**, *566*, 150645. [CrossRef]
24. Li, J.; Wu, P.; Lou, F.; Zhang, P.; Tang, Y.; Zhou, Y.; Lu, T. Mesoporous carbon anchored with SnS₂ nanosheets as an advanced anode for lithium-ion batteries. *Electrochim. Acta* **2013**, *111*, 862–868. [CrossRef]
25. Barkholtz, H.M.; Preger, Y.; Ivanov, S.; Langendorf, J.; Torres-Castro, L.; Lamb, J.; Chalamala, B.; Ferreira, S.R. Multi-scale thermal stability study of commercial lithium-ion batteries as a function of cathode chemistry and state-of-charge. *J. Power Sources* **2019**, *435*, 226777. [CrossRef]
26. Yu, S.; Mao, Y.; Xie, J.; Xu, C.; Lu, T. Thermal runaway chain reaction determination and mechanism model establishment of NCA-graphite battery based on the internal temperature. *Appl. Energy* **2024**, *353*, 122097. [CrossRef]
27. Kim, H.S.; Chung, Y.H.; Kang, S.H.; Sung, Y.-E. Electrochemical behavior of carbon-coated SnS₂ for use as the anode in lithium-ion batteries. *Electrochim. Acta* **2009**, *54*, 3606–3610. [CrossRef]
28. Park, Y.-S.; Lee, S.-M. Effects of particle size on the thermal stability of lithiated graphite anode. *Electrochim. Acta* **2009**, *54*, 3339–3343. [CrossRef]
29. Huang, Y.; Lin, Y.-C.; Jenkins, D.M.; Chernova, N.A.; Chung, Y.; Radhakrishnan, B.; Chu, I.-H.; Fang, J.; Wang, Q.; Omenya, F.; et al. Thermal Stability and Reactivity of Cathode Materials for Li-Ion Batteries. *ACS Appl. Mater. Interfaces*. *ACS Appl. Mater. Interfaces* **2016**, *8*, 7013–7021. [CrossRef]
30. Roth, E.; Doughty, D.; Franklin, J. DSC investigation of exothermic reactions occurring at elevated temperatures in lithium-ion anodes containing PVDF-based binders. *J. Power Sources* **2004**, *134*, 222–234. [CrossRef]
31. Zhang, Z.; Fouchard, D.; Rea, J. Differential scanning calorimetry material studies: Implications for the safety of lithium-ion cells. *J. Power Sources* **1998**, *70*, 16–20. [CrossRef]
32. Liu, X.; Ren, D.; Hsu, H.; Feng, X.; Xu, G.-L.; Zhuang, M.; Gao, H.; Lu, L.; Han, X.; Chu, Z.; et al. Thermal Runaway of Lithium-Ion Batteries without Internal Short Circuit. *Joule* **2018**, *2*, 2047–2064. [CrossRef]
33. Feng, X.; Ouyang, M.; Liu, X.; Lu, L.; Xia, Y.; He, X. Thermal runaway mechanism of lithium ion battery for electric vehicles: A review. *Energy Storage Mater.* **2018**, *10*, 246–267. [CrossRef]
34. Akram, M.; Taha, I.; Ghobashy, M.M. Low temperature pyrolysis of carboxymethylcellulose. *Cellulose* **2016**, *23*, 1713–1724. [CrossRef]
35. Williams, P.T.; Besler, S. Pyrolysis-thermogravimetric analysis of tyres and tyre components. *Fuel* **1995**, *74*, 1277–1283. [CrossRef]
36. Wang, Q.; Sun, J.; Yao, X.; Chen, C. Thermal Behavior of Lithiated Graphite with Electrolyte in Lithium-Ion Batteries. *J. Electrochem. Soc.* **2006**, *153*, A274–A329. [CrossRef]
37. Doi, T.; Zhao, L.; Zhou, M.; Okada, S.; Yamaki, J.-I. Quantitative studies on the thermal stability of the interface between graphite electrode and electrolyte. *J. Power Sources* **2008**, *185*, 1380–1385. [CrossRef]
38. Gachot, G.; Grugeon, S.; Eshetu, G.G.; Mathiron, D.; Ribière, P.; Armand, M.; Laruelle, S. Thermal behaviour of the lithiated-graphite/electrolyte interface through GC/MS analysis. *Electrochim. Acta* **2012**, *83*, 402–409. [CrossRef]

39. Jennifer, V.; Hang, L. Safety Evaluation of Lithium-ion Battery Cathode and Anode Materials Using Differential Scanning Calorimetry. Available online: <https://www.tainstruments.com/applications-notes/safety-evaluation-of-lithium-ion-battery-cathode-and-anode-materials-using-differential-scanning-calorimetry/> (accessed on 5 June 2025).
40. Robert, F.; Lippens, P.; Olivier-Fourcade, J.; Jumas, J.-C.; Gillot, F.; Morcrette, M.; Tarascon, J.-M. Mössbauer spectra as a “fingerprint” in tin-lithium compounds: Applications to Li-ion batteries. *J. Solid State Chem.* **2007**, *180*, 339–348. [CrossRef]
41. Nguyen, C.C.; Yoon, T.; Seo, D.M.; Guduru, P.; Lucht, B.L. Systematic Investigation of Binders for Silicon Anodes: Interactions of Binder with Silicon Particles and Electrolytes and Effects of Binders on Solid Electrolyte Interphase Formation. *ACS Appl. Mater. Interfaces* **2016**, *8*, 12211–12220. [CrossRef]
42. Sopinskyy, M.V.; Khomchenko, V.S.; Strelchuk, V.V.; Nikolenko, A.S.; Olchovsky, G.P.; Vishnyak, V.V.; Stonis, V.V. Possibility of graphene growth by close space sublimation. *Nanoscale Res. Lett.* **2014**, *9*, 182. [CrossRef]
43. Kupka, J.; Surace, Y.; Cupid, D.M.; Flandorfer, H. Understanding and Comparing the Stability of Water-versus NMP-Based Tin(IV)Sulfide Electrodes Using Post-Mortem Analysis. *ChemElectroChem* **2025**, *12*, e202400702. [CrossRef]
44. Sharova, V.; Moretti, A.; Diemant, T.; Varzi, A.; Behm, R.; Passerini, S. Comparative study of imide-based Li salts as electrolyte additives for Li-ion batteries. *J. Power Sources* **2018**, *375*, 43–52. [CrossRef]
45. Böhme, S.; Philippe, B.; Edström, K.; Nyholm, L. Photoelectron Spectroscopic Evidence for Overlapping Redox Reactions for SnO₂ Electrodes in Lithium-Ion Batteries. *J. Phys. Chem. C* **2017**, *121*, 4924–4936. [CrossRef]
46. Kwoka, M.; Ottaviano, L.; Passacantando, M.; Santucci, S.; Czempik, G.; Szuber, J. XPS study of the surface chemistry of L-CVD SnO₂ thin films after oxidation. *Thin Solid Films* **2005**, *490*, 36–42. [CrossRef]
47. Zhang, L.; Li, P.; Zhang, D.; Pei, C.; Sun, B.; Ni, S. Lithium difluoro(oxalate)borate as an efficient and multifunctional additive for extended cycling life of LiFePO₄ cathodes. *Ionics* **2024**, *30*, 2493–2501. [CrossRef]
48. Keefe, A.S.; Weber, R.; Hill, I.G.; Dahn, J.R. Studies of the SEI layers in Li(Ni_{0.5}Mn_{0.3}Co_{0.2})O₂/Artificial Graphite Cells after Formation and after Cycling. *J. Electrochem. Soc.* **2020**, *167*, 120507. [CrossRef]
49. Crist, B.V. Monochromatic XPS Spectra the Elements and Native Oxides. 2024. Available online: <https://xpsmetrology.com> (accessed on 27 March 2025).
50. Fantauzzi, M.; Elsener, B.; Atzei, D.; Rigoldi, A.; Rossi, A. Exploiting XPS for the identification of sulfides and polysulfides. *RSC Adv.* **2015**, *5*, 75953–75963. [CrossRef]
51. Kato, A.; Kowada, H.; Deguchi, M.; Hotehama, C.; Hayashi, A.; Tatsumisago, M. XPS and SEM analysis between Li/Li₃PS₄ interface with Au thin film for all-solid-state lithium batteries. *Solid State Ion.* **2018**, *322*, 1–4. [CrossRef]
52. Ding, R.; Zheng, Y.; Liang, G. Li₂S as a cathode additive to compensate for the irreversible capacity loss of lithium iron phosphate batteries. *Ionics* **2022**, *28*, 1573–1581. [CrossRef]
53. Zha, C.; Wang, S.; Liu, C.; Zhao, Y.; He, B.; Lyu, C.; Li, J.; Ji, S.; Chen, S.; Hui, K.S.; et al. Single-atom tailoring of Li₂S to Form Li₂S₂ for building better lithium-sulfur batteries. *Energy Storage Mater.* **2022**, *47*, 79–86. [CrossRef]
54. Lu, F.; Ji, X.; Yang, Y.; Deng, W.; Banks, C.E. Room temperature ionic liquid assisted well-dispersed core-shell tin nanoparticles through cathodic corrosion. *RSC Adv.* **2013**, *3*, 18791–18793. [CrossRef]
55. Paparazzo, E. On the interpretation of XPS spectra of metal (Pt, Pt-Sn) nanoparticle/graphene systems. *Carbon* **2013**, *63*, 578–581. [CrossRef]
56. Pan, S.S.; Wang, S.; Zhang, Y.X.; Luo, Y.Y.; Kong, F.Y.; Xu, S.C.; Xu, J.M.; Li, G.H. P-type conduction in nitrogen-doped SnO₂ films grown by thermal processing of tin nitride films. *Appl. Phys. A* **2012**, *109*, 267–271. [CrossRef]
57. Szuber, J.; Czempik, G.; Larciprete, R.; Koziej, D.; Adamowicz, B. XPS study of the L-CVD deposited SnO thin films exposed to 2 oxygen and hydrogen. *Thin Solid Films* **2001**, *391*, 198–203.
58. Bulíř, J.; Zíkmund, T.; Novotný, M.; Lančok, J.; Fekete, L.; Juha, L. Photoluminescence excitation of lithium fluoride films by surface plasmon resonance in Kretschmann configuration. *Appl. Phys. A* **2016**, *122*, 1–7. [CrossRef]
59. Crist, V. Tin [Internet]. Tin Basic XPS Information. Available online: <https://xpsdatabase.net/tin-sn-z50-tin-compounds> (accessed on 11 July 2025).
60. Dedryvère, R.; Leroy, S.; Martinez, H.; Blanchard, F.; Lemordant, D.; Gonbeau, D. XPS valence characterization of lithium salts as a tool to study electrode/electrolyte interfaces of Li-ion batteries. *J. Phys. Chem. B* **2006**, *110*, 12986–12992. [CrossRef]
61. Valence Band Spectra—The Elements. Available online: <https://xpslibrary.com/valence-band-spectra-elements/?srsltid=AfmBOor98J3-jhYHNOjWliDb88VvnmmAVhWYmOxOSdWIZ1ljRu0GSLzF> (accessed on 11 July 2025).
62. Isaacs, M. Knowledge Base (Tin). Available online: <https://www.harwellxps.guru/knowledgebase/tin/#1703157303003-17a320fc-c273e144-93715127-1815f90a-7b0d43aa-31eba8a-9f85> (accessed on 11 July 2025).
63. Zatsepин, D.; Zatsepин, A.; Boukhvalov, D.; Kurmaev, E.; Gavrilov, N. Sn-loss effect in a Sn-implanted a-SiO₂ host-matrix after thermal annealing: A combined XPS, PL, and DFT study. *Appl. Surf. Sci.* **2016**, *367*, 320–326. [CrossRef]
64. Schwöbel, A.; Precht, R.; Motzko, M.; Solano, M.A.C.; Calvet, W.; Hausbrand, R.; Jaegermann, W. Determination of the valence band structure of an alkali phosphorus oxynitride glass: A synchrotron XPS study on LiPON. *Appl. Surf. Sci.* **2014**, *321*, 55–60. [CrossRef]

65. Dedryvère, R.; Laruelle, S.; Grugeon, S.; Gireaud, L.; Tarascon, J.-M.; Gonbeau, D. XPS Identification of the Organic and Inorganic Components of the Electrode/Electrolyte Interface Formed on a Metallic Cathode. *J. Electrochem. Soc.* **2005**, *152*, A689–A696. [[CrossRef](#)]
66. Gao, T.; Bai, J.; Ouyang, D.; Wang, Z.; Bai, W.; Mao, N.; Zhu, Y. Effect of aging temperature on thermal stability of lithium-ion batteries: Part A—High-temperature aging. *Renew. Energy* **2023**, *203*, 592–600. [[CrossRef](#)]
67. An, S.J.; Li, J.; Daniel, C.; Mohanty, D.; Nagpure, S.; Wood, D.L. The state of understanding of the lithium-ion-battery graphite solid electrolyte interphase (SEI) and its relationship to formation cycling. *Carbon* **2016**, *105*, 52–76. [[CrossRef](#)]
68. Andersson, A.; Herstedt, M.; Bishop, A.; Edström, K. The Influence of Lithium Salt on the Interfacial Reactions Controlling the Thermal Stability of Graphite Anodes. *Electrochim. Acta* **2002**, *47*, 1885–1898. [[CrossRef](#)]
69. Aupperle, F.; von Aspern, N.; Berghus, D.; Weber, F.; Eshetu, G.G.; Winter, M.; Figgemeier, E. The Role of Electrolyte Additives on the Interfacial Chemistry and Thermal Reactivity of Si-Anode-Based Li-Ion Battery. *ACS Appl. Energy Mater.* **2019**, *2*, 6513–6527. [[CrossRef](#)]
70. Wang, Q.; Sun, J.; Chen, C. Effects of solvents and salt on the thermal stability of lithiated graphite used in lithium ion battery. *J. Hazard. Mater.* **2009**, *167*, 1209–1214. [[CrossRef](#)]
71. Ryou, M.-H.; Lee, J.-N.; Lee, D.J.; Kim, W.-K.; Jeong, Y.K.; Choi, J.W.; Park, J.-K.; Lee, Y.M. Effects of lithium salts on thermal stabilities of lithium alkyl carbonates in SEI layer. *Electrochim. Acta* **2012**, *83*, 259–263. [[CrossRef](#)]
72. Yoon, T.; Milien, M.S.; Parimalam, B.S.; Lucht, B.L. Thermal Decomposition of the Solid Electrolyte Interphase (SEI) on Silicon Electrodes for Lithium Ion Batteries. *Chem. Mater.* **2017**, *29*, 3237–3245. [[CrossRef](#)]
73. Wu, J.; Weng, S.; Zhang, X.; Sun, W.; Wu, W.; Wang, Q.; Yu, X.; Chen, L.; Wang, Z.; Wang, X. In Situ Detecting Thermal Stability of Solid Electrolyte Interphase (SEI). *Small* **2023**, *19*, e2208239. [[CrossRef](#)]
74. Zu, C.; Yu, H.; Li, H. Enabling the thermal stability of solid electrolyte interphase in Li-ion battery. *InfoMat* **2021**, *3*, 648–661. [[CrossRef](#)]
75. Kim, J.; Gil Lee, J.; Kim, H.-S.; Lee, T.J.; Park, H.; Ryu, J.H.; Oh, S.M. Thermal Degradation of Solid Electrolyte Interphase (SEI) Layers by Phosphorus Pentafluoride (PF 5) Attack. *J. Electrochem. Soc.* **2017**, *164*, A2418–A2425. [[CrossRef](#)]
76. Veith, G.M.; Doucet, M.; Sacci, R.L.; Vacaliuc, B.; Baldwin, J.K.; Browning, J.F. Determination of the Solid Electrolyte Interphase Structure Grown on a Silicon Electrode Using a Fluoroethylene Carbonate Additive. *Sci. Rep.* **2017**, *7*, 6326. [[CrossRef](#)]
77. Fears, T.M.; Doucet, M.; Browning, J.F.; Baldwin, J.K.S.; Winiarz, J.G.; Kaiser, H.; Taub, H.; Sacci, R.L.; Veith, G.M. Evaluating the solid electrolyte interphase formed on silicon electrodes: A comparison of: Ex situ X-ray photoelectron spectroscopy and in situ neutron reflectometry. *Phys. Chem. Chem. Phys.* **2016**, *18*, 13927–13940. [[CrossRef](#)] [[PubMed](#)]
78. Menachem, C.; Golodnitsky, D.; Peled, E. Effect of mild oxidation of natural graphite (NG7) on anode-electrolyte thermal reactions. *J. Solid State Electrochem.* **2001**, *5*, 81–87. [[CrossRef](#)]
79. El Moutchou, S.; Aziam, H.; Mansori, M.; Saadoune, I. Thermal stability of Lithium-ion batteries: Case study of NMC811 and LFP cathode materials. *Mater. Today Proc.* **2021**, *51*, A1–A7. [[CrossRef](#)]
80. He, R.; Guo, B.; Li, Y.; Yang, S. Revealing the impact of extreme temperatures and dynamic conditions on thermal safety of NCA/Si-graphite battery. *Energy* **2025**, *324*, 136043. [[CrossRef](#)]

Disclaimer/Publisher’s Note: The statements, opinions and data contained in all publications are solely those of the individual author(s) and contributor(s) and not of MDPI and/or the editor(s). MDPI and/or the editor(s) disclaim responsibility for any injury to people or property resulting from any ideas, methods, instructions or products referred to in the content.